

Wall-Resolved Large Eddy Simulations of Transonic Shock-Induced Flow Separation

Ali Uzun *

National Institute of Aerospace, Hampton, VA 23666

Mujeeb R. Malik †

NASA Langley Research Center, Hampton, VA 23681

This paper reports the wall-resolved large eddy simulations of shock-induced boundary layer separation over an axisymmetric bump for a flow Mach number of 0.875 and a chord-based Reynolds number of 2.763 million. The incoming boundary layer has a momentum-thickness Reynolds number of 6600 at one and a half chord lengths upstream of the leading edge. The calculations simulate the experiment by Bachalo and Johnson (*AIAA Journal*, Vol. 24, No. 3, 1986), except that the tunnel walls are ignored and the simulations are performed assuming free air with as many as 24 billion grid points. The effects of domain span, grid resolution and time step on the predictions are examined. The results are found to show some sensitivity to the studied parameters. Owing to the outer boundary conditions, the predicted surface pressure distribution as well as the flow separation and reattachment locations tend to agree better with the experimental results from the larger (6 × 6 ft) tunnel than those from the smaller (2 × 2 ft) tunnel. The predicted Reynolds shear stress profiles in the separated region differ by as much as 31% from the experimental results that were only obtained in the smaller tunnel. The most accurate surface pressure distribution obtained in this study lies within the scatter of the measurements taken in the two facilities.

I. Introduction

Accurate prediction of smooth-body flow separation remains a subject of ongoing investigation because of its relevance to many technological applications. The turbulence research community is actively engaged in evaluating a number of computational strategies of varying degrees of fidelity for separated flows. Robust simulation tools that accurately predict flow separation in various configurations can help develop improved designs and control strategies to counteract the adverse effects of separation, such as increased aerodynamic drag, stall and reduced system performance. High Reynolds number separated flow problems are generally difficult to predict and have been mostly studied using techniques such as Reynolds-averaged Navier-Stokes (RANS) calculations, wall-modeled large-eddy simulations (WMLES) or hybrid RANS-LES type approaches. In the case of RANS, available turbulence models commonly fail to properly account for nonequilibrium effects in separated flows. An example demonstrating the failure of RANS in the well-known NASA wall-mounted hump test case can be found in the paper by Rumsey et al.¹ This commonly studied benchmark problem involves low-speed flow separation due to an adverse pressure gradient generated by a change in body contour in the aft portion of the hump. RANS has been found to significantly overpredict the separation-bubble length in this problem by as much as 35%, which is deemed unacceptable for design purposes. This failure of RANS has resulted in increased interest toward the use of scale-resolving approaches for the computation of separated flows. For example, for the NASA hump problem, WMLES studies by several groups²⁻⁶ have reported generally better success than RANS but still exhibited some deficiencies in the overall skin-friction prediction, which is considered an important quantity of interest in aerodynamic design.

Although WMLES has seen recent widespread use in a number of problems, an important matter that has not been properly addressed by the community is the potential presence of multiple error sources in a typical WMLES calculation, in which the grid resolutions outside the wall-modeled region might be much too coarse for LES. The main justification for this practice appears to be the desire to speed up the computations in the face of limited computing power. However, given a particularly high Reynolds number, this approach will inevitably put too much reliance on

*Senior Research Scientist, Senior Member AIAA.

†Senior Aerodynamicist, Computational AeroSciences Branch, MS 128, Fellow AIAA.

the subgrid-scale models to properly account for a significant range of energy-containing scales not resolved by the LES grid. Hence, there are at least two sources of error in most WMLES: the error of the particular wall model used in the near-wall region and the error coming from the coarse grid resolution used in the outer region. Moreover, the number of grid points across the boundary layer might be too few, particularly in regions containing a strong favorable pressure gradient. Additionally, the computational time step might be considerably greater than the smallest physical time scales present in the LES region, and this will constitute another source of error despite allowing a numerically stable computation. Insufficient span size in simulations that assume spanwise periodicity could be yet another source of error, particularly in separated flows. Further studies are therefore needed in order to address these potential sources of error in WMLES. A parametric study regarding the effect of grid resolution, time step and span size is carried out in the present work using wall-resolved large eddy simulation (WRLES). This will hopefully set a precedent that will motivate the WMLES community to perform similar parametric studies, which should be feasible given the much lower computational cost of WMLES compared to WRLES.

While the NASA hump problem is a useful test case for low-speed flow separation, a more relevant problem involves the shock-induced boundary layer separation observed under transonic flow conditions. This phenomenon commonly occurs in a number of practical applications where the adverse pressure gradient generated by the presence of a shock, potentially further augmented by a change in body contour, causes flow separation. The experiment by Bachalo and Johnson⁷ investigates the shock-induced boundary layer separation over an axisymmetric bump that is representative of the upper surface of a transonic airfoil, as depicted in figure 1 and reported on the NASA turbulence modeling resource website (<http://turbmodels.larc.nasa.gov>^a). Despite its failure in the NASA wall hump problem, RANS with the Shear Stress Transport (SST) model was found to provide reasonable predictions in the Bachalo-Johnson flow but some differences relative to the experimental observation still remained. The better performance of the SST model in this problem is not surprising since the data from the Bachalo-Johnson experiment was used in the calibration of the model coefficients.

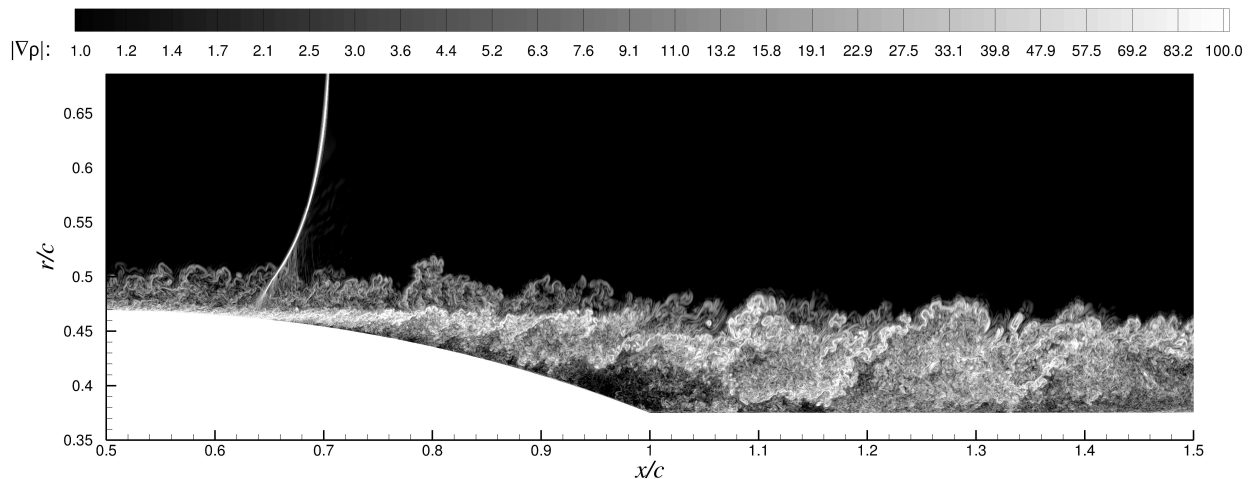


Figure 1. Numerical schlieren (depicted in terms of normalized density gradient magnitude) visualizing shock-induced flow separation in Bachalo-Johnson flow. The axial and radial distances are scaled by the bump chord length, c . (Figure generated using the simulation data from the present study.)

To our knowledge, Spalart et al.^{8,9} are the first group that used WMLES to study the Bachalo-Johnson flow. Their WMLES methodology is the same as that by Shur et al.,³ which reported good success in the NASA wall-mounted hump problem. Despite this success, the same methodology faced difficulty in correctly computing the shock location in the Bachalo-Johnson flow.^{8,9} This suggests that a particular wall model that works well under certain flow conditions may fail under different flow conditions. The incorrect prediction of the shock position by WMLES in the Bachalo-Johnson flow^{8,9} leads to incorrect flow separation and reattachment locations. Faced with the difficulty of accurately predicting the shock position in a WMLES performed using nearly 1.7 billion grid points, Spalart et al.^{8,9} had to resort to a hybrid simulation (with about 8.45 billion points) in which the attached flow region was computed using direct numerical simulation (DNS) while the separated region had to be simulated using delayed detached eddy simulation (DDES) due to computational resource limitations. This hybrid simulation, which covered only 15 degrees of azimuth, was able to improve the shock position prediction. These observations highlight the daunting challenge associated with

^aWebsite last accessed 31 August 2017.

the prediction of separated flows and indicate that even a very large number of grid points used for a complex flow separation problem does not guarantee that the flowfield will be predicted accurately with wall-modeled approaches.

These observations coupled with the mixed success of WMLES in separated flows motivated us to embark on a systematic study exploring the use of higher-fidelity wall-resolved LES (WRLES) for the two benchmark problems discussed above. We have made significant strides in this regard. The results from the application of WRLES to the NASA hump model were discussed in recent papers.^{10,11} The Bachalo-Johnson problem is studied in the present paper, where we have performed wall-resolved simulations on grids containing as many as 24 billion points with a high-order compact finite-difference scheme. The main findings reported in this paper include the effects of azimuthal domain, grid resolution and time step on the simulation predictions. The paper is organized as follows. Section II summarizes the computational methodology employed in this study. The details of the experiment and the computational setup are discussed in sections III.A and III.B, respectively. The analysis of the simulation results are presented in section III.C. Section IV provides a summary of the findings and the concluding remarks.

II. Computational Methodology

The code used in the present study solves the unsteady three-dimensional compressible Navier-Stokes equations discretized on multiblock structured and overset grids. It employs an optimized prefactored fourth-order accurate compact finite-difference scheme¹² to compute all spatial derivatives in the governing equations. This optimized scheme offers improved dispersion characteristics compared to the standard sixth- and eighth-order compact schemes.¹³ Third-order one-sided and biased schemes, respectively, are used on a boundary point and on the point next to the boundary. To eliminate the spurious high-frequency numerical oscillations that may arise from several sources (such as grid stretching, unresolved length scales and approximation of physical boundary conditions) and ensure numerical stability during the simulation, we also employ a sixth-order compact filtering scheme.^{14,15} The flow solver also has overset grid capability, which is useful in meshing complex geometries and avoiding grid point singularities. To maintain high-order accuracy throughout the entire computational domain, we perform a sixth-order accurate explicit Lagrangian interpolation¹⁶ whenever overset grids are used. Shock-capturing is accomplished by means of adaptive artificial dissipation,¹⁷ which is only added in the vicinity of shocks. A special shock sensor, similar to that proposed by Ducros et al.,¹⁸ identifies the shock-containing regions to which adaptive artificial dissipation is applied. A Beam-Warming type approximately factorized implicit scheme with subiterations is used for the time advancement.¹⁹ More details of the simulation methodology can be found in the publications by Uzun and coworkers.^{20–25}

Instead of using an explicit subgrid-scale (SGS) model, the numerical dissipation of the sixth-order compact filtering scheme^{14,15} is chosen to serve as an implicit SGS model. This sixth-order filter was preferred over higher-order filters (such as eighth- or tenth-order) because of its robustness in a number of problems studied previously. However, work is currently underway to evaluate the stability of higher-order filters on the present grids and determine the sensitivity of results to the order of filtering scheme. These findings will be reported in the future.

III. Test Case: Transonic Shock-Induced Flow Separation

The problem of interest involves the shock-induced boundary layer separation over an axisymmetric bump mounted on a straight cylinder, representative of the upper surface of a transonic airfoil. A schematic of the axisymmetric bump is shown in Figure 2(a). As depicted in figure 2(b), the axisymmetric bump is a simple circular arc of radius R_1 , which is smoothly blended to the upstream cylinder with a leading-edge fillet of radius, R_2 . Note that the radius of the circular arc, R_1 , is determined by the bump thickness, t , and the chord length, c . In the references describing the model geometry, there is some uncertainty regarding the tangency points of the fillet and two potential values of R_2 could be discerned: 18.30 cm or 20.32 cm. The bump leading-edge fillet radius could have an important effect on the results as it determines how fast the flow accelerates over the front portion of the bump. In the absence of absolute knowledge, and to facilitate comparison with the results of Spalart et al.,^{8,9} we use the value chosen by them, which is $R_2 = 18.30$ cm. This allows a more meaningful comparison with their results. Table 1 gives the dimensions of the geometric parameters that describe the bump shape used in the present study.

Figure 3 provides the experimental surface oil flow pattern obtained in the NASA Ames 2×2 ft transonic tunnel. While the oil flow depicts a straight separation line, further examination shows that there might be some azimuthal variation in the reattachment line, which is the boundary between the gray zone (depicting the separated region) and the darker zone downstream of it (depicting the reattachment region). Note that the upper and lower walls of this tunnel are porous while the other two walls are solid. The shortest distance between the tunnel walls and the model centerline is only $1.5c$ or $2d$. Hence, the combination of the relatively small tunnel size and the “nonuniformity” of

Table 1. Geometric parameters of the axisymmetric bump used in the present work.

Leading-edge fillet radius, R_2	Bump chord, c	Bump thickness, t	Arc radius, R_1	Cylinder diameter, d
18.30 cm	20.32 cm	1.905 cm	$0.5(t^2 + 0.25c^2)/t$	15.24 cm

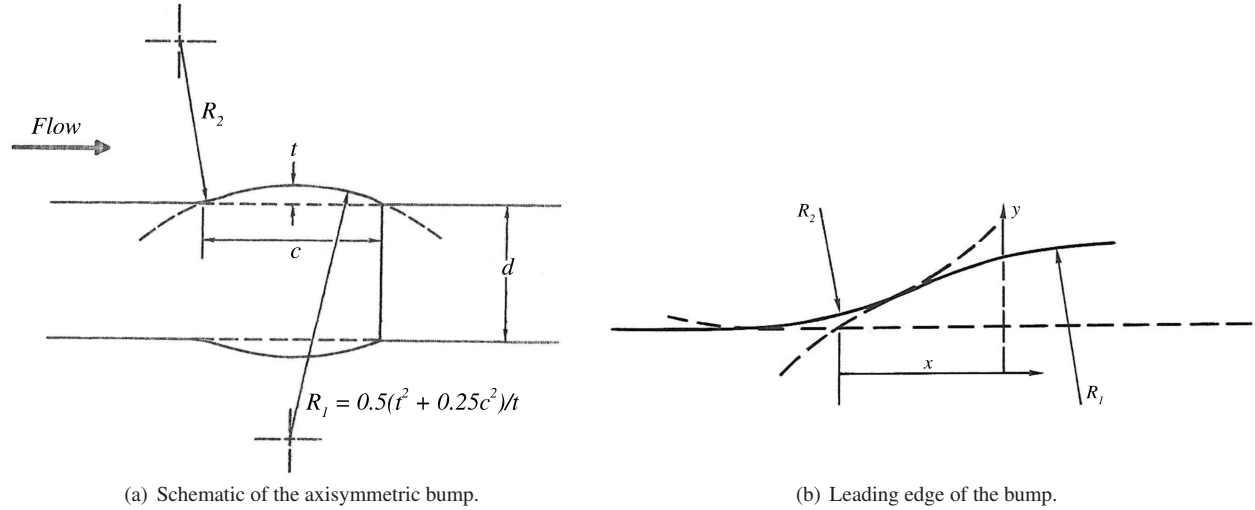


Figure 2. Schematic of the axisymmetric bump geometry and its leading-edge details.

the square tunnel wall boundary conditions might have introduced some azimuthal variation in certain flow features.

The estimated boundary layer momentum-thickness Reynolds number at $1.5c$ upstream of the leading edge is $Re_\theta \approx 6600$. The freestream Mach number is 0.875. The Reynolds number based on c and the freestream velocity, u_∞ , is $Re_c = 2.763$ million. The transonic flow condition gives rise to the formation of a shock in the aft region of the bump. The interaction of this shock with the turbulent boundary layer results in boundary layer separation, which is depicted in figure 1 based on the current simulation results. Next, we discuss the relevant details of the experiment before analyzing the simulation results.

A. The Bachalo-Johnson Experiment

The original experimental tests were conducted at NASA Ames in the late 1970s and led to a number of papers^{7,26–30} published mostly in the 1980s. The 1986 paper by Bachalo and Johnson⁷ is generally considered to be the main reference for the problem of interest. The experimental results discussed in this paper were collected in a 2×2 ft transonic tunnel with porous upper and lower walls. Figure 2 from Bachalo and Johnson,⁷ reproduced here as figure 4, gives the flow separation and reattachment in this tunnel at $x/c \approx 0.7$ and 1.1, respectively, for a freestream Mach number of 0.875. In addition to the surface pressure and oil flow measurements, mean flowfield and Reynolds stress data were taken in the 2×2 ft tunnel experiment. Bachalo and Johnson⁷ mention that the experiment was also repeated in a 6×6 ft supersonic tunnel with solid walls and both tunnel tests result in a similar surface pressure distribution. Regarding this point, page 439 of Bachalo and Johnson⁷ states that: “*Subsequent tests in the Ames 6×6 ft wind tunnel indicated a similar surface pressure distribution. This agreement alleviated the concern with wind tunnel wall effects on the interaction.*” However, as indicated below, this statement is not fully supported by a careful comparison of the results from the two experiments.

Some discussion of the experiment repeated in the 6×6 ft supersonic tunnel with solid walls can be found in the related publications by Horstman and Johnson²⁸ and Johnson.^{29,30} Only the surface pressure distribution and oil flow measurements were gathered in the 6×6 ft tunnel. Figure 3 from Horstman and Johnson,²⁸ reproduced here as figure 5, plots the variation of separation and reattachment locations with the freestream Mach number in the large tunnel. For the freestream Mach number of 0.875, we observe that the separation point is in the vicinity of $x/c \approx 0.66 - 0.69$

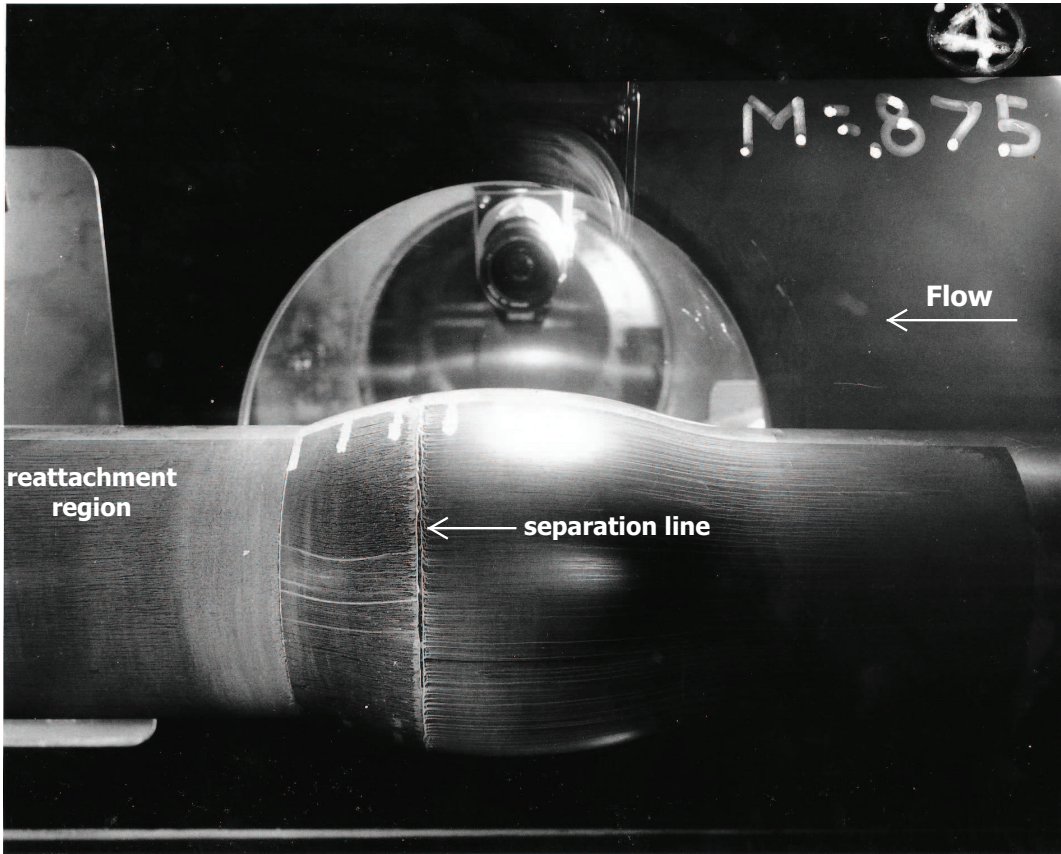


Figure 3. Surface oil flow pattern (courtesy of Dr. Dennis Johnson) in the NASA Ames 2×2 ft transonic tunnel at Mach 0.875.

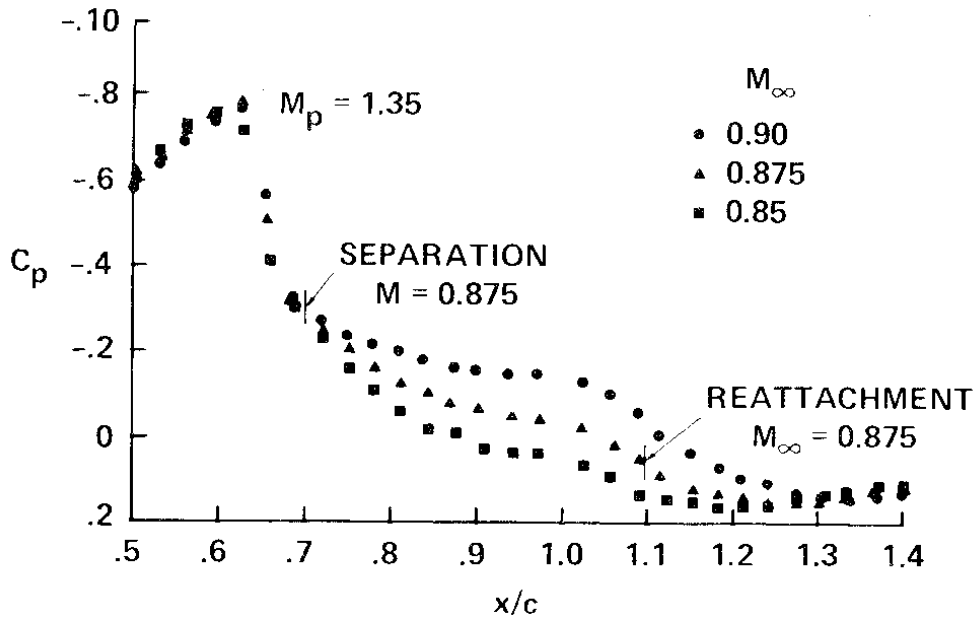


Figure 4. Surface pressure data taken in the 2×2 ft tunnel at various freestream Mach numbers.

and the reattachment location is at $x/c \approx 1.17$. We believe the separation point in the large tunnel to be closer to $x/c \approx 0.69$ based on the shock location in the measured surface pressure distribution. As noted above, for the experiment conducted in the 2×2 ft tunnel,⁷ the separation and reattachment locations were found to be at $x/c \approx 0.7$ and 1.1, respectively, from the surface oil flow measurement. The separation-bubble length in the small and large tunnels is thus about $0.4c$ and $0.48c$, respectively. This translates to a 20% difference in the separation-bubble length between the two facilities, which shows that there is considerable effect of the tunnel size and hence wall boundary conditions.

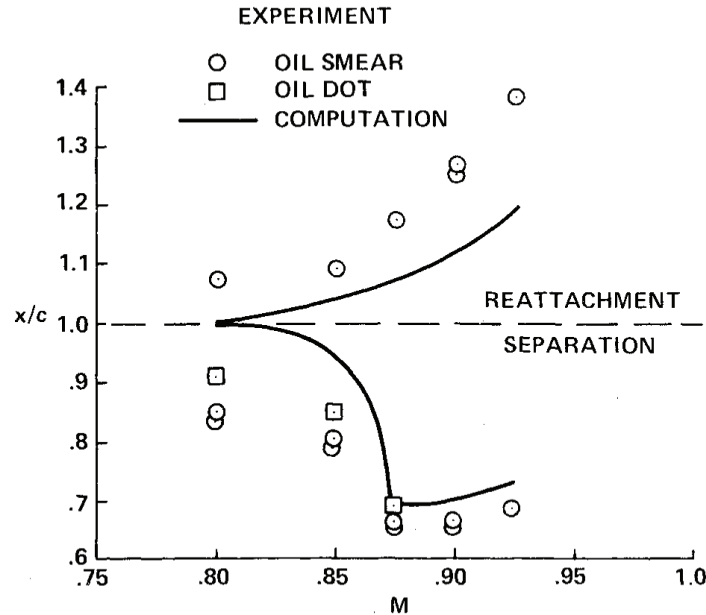


Figure 5. Figure 3 from Horstman and Johnson²⁸ showing the variation of separation and reattachment locations with freestream Mach number in the 6×6 ft tunnel.

B. Simulation Details

The experimental Mach number and Reynolds number are exactly matched in our wall-resolved simulations. Since a wall-resolved simulation of the entire axisymmetric bump is prohibitively expensive, we consider an azimuthal portion of the axisymmetric body with periodic boundary conditions applied on the edges of the slice. A lesson learned from our previous work on the NASA wall hump problem^{10,11} was that the domain span in a spanwise-periodic calculation can have a significant effect on the growth of the separated shear layer, whose dynamics is governed by the large-scale structures developing in the shear layer, and the subsequent flow reattachment location. A narrow span can constrain the growth of large structures and significantly alter the reattachment location. The effect of domain span on the numerical predictions is studied by considering 30, 60 and 120 degree slices of the full geometry.

The differences between the small and large tunnel measurements discussed earlier were not noticed prior to initiating the computational work in this study. Because of this oversight, the tunnel wall effect was assumed negligible and therefore ignored in the simulations. In any case, only the upper and lower walls of the 2×2 ft transonic tunnel were porous and the side walls were solid. As in Spalart et al.,^{8,9} who also ignored the tunnel walls, the outer boundary conditions are imposed at $r/c = 10$. Figure 6 depicts a schematic of the computational domain assuming free air and the boundary conditions applied on the domain boundaries. The leading edge of the bump geometry is at $x/c = 0$. The inflow boundary is placed at $x/c = -1.5$ while the outflow boundary is placed at $x/c = 10$. The physical domain of interest ends at $x/c = 2$. The region from $x/c = 2$ to 10 is the sponge zone, which is constructed using about 200 points with rapid grid stretching applied in the axial direction. The grid stretching in the sponge zone is augmented with additional filtering that is applied in the vicinity of the outflow boundary so that the turbulence is completely damped out before it reaches the domain exit. The outer freestream boundary is located at $r/c = 10$. Characteristic boundary conditions are imposed on the freestream and outflow boundaries. The mean flow imposed at the inflow boundary of the simulation is taken from the RANS performed by Spalart et al.^{8,9} using the SST model. The mean boundary layer thickness on the inflow boundary is $\delta_{in} \approx 0.0213c$. To reiterate, this corresponds to $Re_{\theta} \approx 6600$.

The turbulent fluctuations imposed on the mean inflow profile are generated using a modified version of the rescaling-recycling technique, described in Uzun and Malik.¹¹ This inflow generation method also includes several modifications proposed by Morgan et al.³¹ to eliminate possible energetic low frequencies that may be artificially introduced by the turbulent inflow generation technique. The distance between the inflow and recycle planes is taken as $15 \delta_{in}$. Adiabatic viscous wall boundary conditions are imposed on the cylinder and bump surfaces.

In the small and large tunnel experiments, the shortest distance between the tunnel wall and the cylinder centerline is $1.5c$ and $4.5c$, respectively. In terms of the cylinder diameter, d , these distances correspond to $2d$ and $6d$, respectively. As the tunnel walls are positioned further away from the model in the large tunnel, the wall interference effect is presumably diminished in the large facility. We therefore expect the simulations performed in free air to be in better agreement with the measurements taken in the large tunnel. Spalart et al.^{8,9} also performed their simulations in free air with the same freestream boundary location as in the present study. This should facilitate a meaningful comparison between the two simulations. Recent RANS calculations by Iyer³² showed that slip wall and characteristic farfield boundary conditions applied at $r/c = 10$ gave identical results, which suggests that tunnel walls would not have any significant effect if the experiment were to be performed in such a large tunnel.

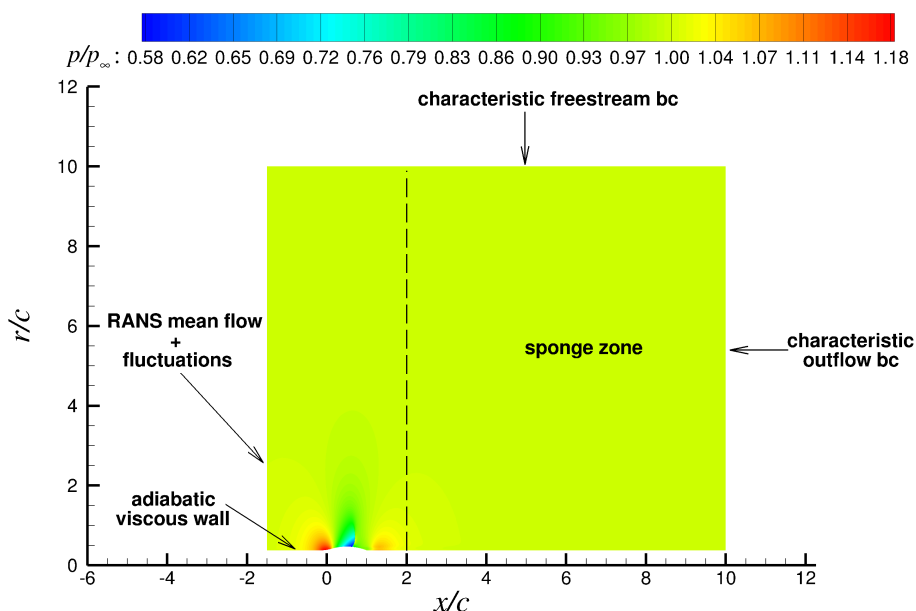


Figure 6. Schematic of the computational domain. Contours denote the mean pressure normalized by the ambient pressure.

A baseline grid, which contains 1 billion points per 10 degrees, and a refined grid, which contains 2 billion points per 10 degrees, are considered in the present study. Both grids employ a two-level overset grid strategy in which the region near the wall is resolved using a fine grid and a coarser grid is used in the outer region. The overset grids communicate by means of sixth-order accurate interpolation in the overlap region. In the baseline grid, the near-wall fine grid typically extends up to $r^+ \approx 200$ in the radial direction in the attached region. In wall units, it has a resolution of $\Delta x^+ \leq 28$ in the streamwise direction and $r\Delta\theta^+ \leq 16$ in the azimuthal direction in the shock-free region. The grid clustering in the vicinity of the shock makes Δx^+ as small as 2–3 in that region. The outer region grid is coarsened by a factor of two both in the streamwise and spanwise directions. The near-wall grid contains about 100 points in the radial direction and the first grid point off the wall generally satisfies $r^+ \leq 1$. The outer grid contains about 400 grid points total in the radial direction with the majority of points located within the region of turbulence-containing eddies. The grid is gradually stretched along the radial direction away from the wall. The radial grid spacing in the boundary layer edge vicinity generally satisfies $\Delta r^+ \leq 40$.

The refined grid is derived from the baseline grid. The near-wall high-resolution grid, maintained until $r^+ \approx 200$ in the baseline grid, is extended further away from the wall to cover the entire turbulent boundary layer and the separated region. The radial grid point distribution in the refined grid is the same as that in the baseline grid. In other words, the total number of radial grid points (split between the near-wall and outer regions) is kept the same as that in the baseline case. In the refined grid case, the near-wall and outer region overset grids contain about 350 and 150 points in the radial direction, respectively. The smallest grid used in the present study contains 3 billion points (baseline grid

with 30 degree span) and while the largest one contains 24 billion points (refined grid with 120 degree span). All calculations are run as implicit LES (ILES). To reiterate, the hybrid DNS-DDES of Spalart et al.^{8,9} that we will make comparisons with, used about 8.45 billion points total and considered an azimuthal slice of 15 degrees.

To study the effect of time step on the predictions, two time steps are chosen. The original nondimensional time step is set to $\Delta t a_\infty / c = 5 \times 10^{-5}$, where a_∞ is the freestream sound speed. This translates to a maximum Courant-Friedrichs-Lewy (CFL) number of about 6 in the thinnest cells next to the wall. The CFL number is computed using the sum of the local mean velocity and the mean sound speed. A second time step, which is equal to one half of the original time step, is also considered. The simulations are normally run for an initial period of 5 to 10 chord flow times before statistical information is gathered. One chord flow time unit, c/u_∞ , is defined as the time it takes for the freestream flow speed, u_∞ , to travel one chord length, c . Statistical data have been gathered over as long as 10 chord flow times depending on the grid size and the time step. The exact duration of the statistical sample size for each case is noted later when the results are presented. Because of the assumed mean flow axisymmetry, statistical results are averaged both in time and along the azimuthal span.

Simulations have been performed using up to 42 thousand cores on the Edison system and up to 170 thousand cores on the Cori system of the National Energy Research Scientific Computing Center (see <http://www.nersc.gov>^b). Edison contains two Intel Ivy Bridge processors (with a total of 24 cores) per node running at 2.4 GHz, while Cori contains a single Intel Knights Landing processor (with a total of 68 cores) per node running at 1.4 GHz. The flow solver runs at approximately the same speed with the same number of nodes on both systems. On Cori, at the half time step, the simulation on the 24 billion point grid takes about 9 days to compute 5 chord flow time units.

C. Simulation Results

We now discuss the simulation results. The details of the turbulent boundary layer upstream of the transonic bump are studied first. The effects of domain span, grid resolution and time step on the predictions are investigated next. Other features of the flow, such as the acceleration region over the bump and the two-point azimuthal correlations upstream and downstream of flow separation, are also analyzed. Finally, comparisons of the velocity and Reynolds shear stress profiles are made with the available experimental measurements.

1. Properties of the Upstream Boundary Layer

We first examine the characteristics of the upstream turbulent boundary layer approaching the transonic bump. The results shown here are from our best-resolved simulation, which is the 24 billion grid case with 120-degree span that was run at the halved time step ($\Delta t a_\infty / c = 2.5 \times 10^{-5}$). As mentioned earlier, the inflow plane in the calculation is placed at $x/c = -1.5$, where the mean flowfield profiles available from a RANS^{8,9} (with the SST model) are imposed. The turbulent fluctuations imposed on the inflow plane are generated using a rescaling-recycling technique, as mentioned earlier. Figure 7(a) shows the mean RANS velocity profile imposed on the inflow boundary and the mean velocity profiles at the axial stations of $x/c = -1, -0.5$ and -0.25 in wall units. For some reason, the RANS mean profile does not appear to have a logarithmic layer. The inflow boundary of this RANS^{8,9} was placed at $x/c = -13$. A slip-wall boundary condition was specified on the cylinder surface until $x/c = -3$, downstream of which a viscous wall boundary condition was applied. Perhaps the distance from $x/c = -3$ to -1.5 is not sufficient for a logarithmic layer to develop in the RANS solution. The mean velocity profile taken from the RANS at $x/c = -1.5$ and specified on our inlet boundary is initially subjected to a relatively mild adverse pressure gradient, which becomes progressively more severe as the leading edge of the bump is approached. Figure 7(b) depicts the surface pressure coefficient variation in the region upstream of the leading edge (see equation 1 for the definition of the pressure coefficient). The distance from the inflow plane to the bump leading edge is on the order of $70 \delta_{in}$. In spite of the questions regarding the initial RANS profile, figure 7(a) suggests that a logarithmic layer quickly begins to develop in the LES.

Figure 8 plots the power spectral density (PSD) of the streamwise velocity fluctuations versus the Strouhal frequency, $St = fc/u_\infty$ (where f is the frequency), within the turbulent boundary layer at $x/c = -1$. This particular station is positioned within the relatively mild adverse pressure gradient region. It is also located about $23.5 \delta_{in}$ downstream of the inflow boundary, thus it should be a useful location to check whether the well-established hallmarks of fully-developed turbulence in a zero pressure-gradient boundary layer exist in the present case. The radial distance from the wall at this PSD location is equal to $\Delta r/\delta = 0.7$, where δ is the local boundary layer thickness. This particular wall distance is chosen so that it is not too close to the wall to be strongly influenced by the wall effects, yet it is also sufficiently away from the boundary layer edge to avoid the intermittency effects. The spectrum is computed

^bWebsite last accessed 28 August 2017.

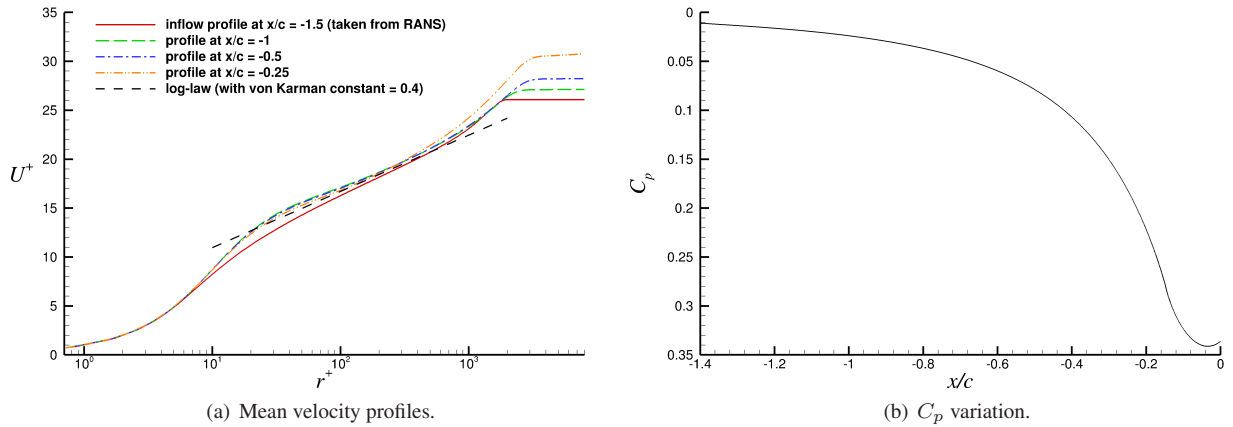


Figure 7. Mean velocity profiles at several stations and surface pressure coefficient (C_p) variation upstream of the leading edge.

using unsteady data gathered over about 4 chord flow times. It displays a typical relatively flat low-frequency range and possesses an inertial range that appears to follow Kolmogorov's $-5/3$ power scaling. In the very high frequency range, the energy decay appears to be proportional to Sr^{-7} ; however, this is only over a fraction of a decade of frequency. Different power-law scalings (such as -6 or -8) might also show a reasonable fit over this relatively short frequency range. Nevertheless, the -7 power decay is the expected behavior in the viscous dissipation range.³³ The observation made in this frequency range of the spectrum suggests that the grid resolution at this particular position within the boundary layer might be fine enough to extend partway into the dissipation range. Similar observations with the same power scalings ($-5/3$ in the inertial range and -7 in the dissipation range) were made in Klebanoff's incompressible flat-plate turbulent boundary layer measurements.^{33,34} Finally, the absence of a particularly energetic discrete low frequency confirms that the turbulent inflow generation technique employed in the present study does not artificially generate spurious low-frequency motions within the boundary layer.

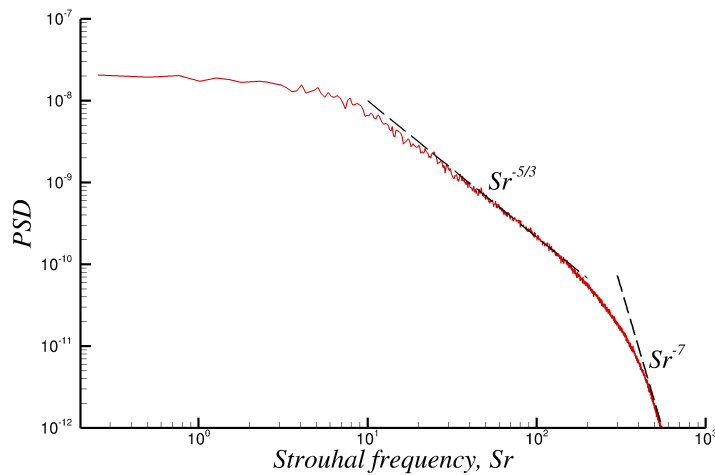


Figure 8. PSD of the streamwise velocity fluctuations at $x/c = -1$ and $\Delta r/\delta = 0.7$.

2. Effect of Azimuthal Span

We now study the effect of azimuthal span on the simulated flow. For this purpose, three simulations are carried out using the baseline grid resolution and the azimuthal span set to 30, 60 and 120 degree slices of the full geometry. The corresponding number of grid points in these simulations is 3, 6 and 12 billion, respectively. All statistical results shown here have been averaged over 10 chord flow time units.

Figure 9 shows the pressure and skin-friction coefficient distributions from our three WRLES solutions and the comparison with the hybrid DNS-DDES result of Spalart et al.^{8,9} Experimental results from the 2×2 ft tunnel are also included in the pressure coefficient comparison. No skin friction measurements were taken in the experiment. The pressure and skin-friction coefficients are defined as

$$C_p = \frac{p - p_\infty}{\frac{1}{2}\rho_\infty u_\infty^2} \quad \text{and} \quad C_f = \frac{\tau_w}{\frac{1}{2}\rho_\infty u_\infty^2} \quad (1)$$

where ρ and p , respectively, are the density and pressure, τ_w is the viscous wall shear stress and the subscript ∞ denotes the reference freestream conditions. The wall shear stress is computed from the temporally and azimuthally averaged mean flow.

We note that the hybrid DNS-DDES of Spalart et al.,^{8,9} which was performed on a 15-degree slice, was averaged over a shorter time of $2.5c/u_\infty$. As can be seen in figure 9(a), the present WRLES and the hybrid DNS-DDES of Spalart et al.^{8,9} predict a shock location similar to that observed in the 2×2 ft tunnel. We observe here that the azimuthal span has a relatively small effect on the C_p predictions on the baseline grid. Some differences between the WRLES predictions and the experimental measurement are evident in the post-shock region. WRLES agrees well with the hybrid DNS-DDES in the attached region and in the shock vicinity, with small differences observed around the bump leading edge. Some differences between the WRLES and the hybrid DNS-DDES are also seen in the post-shock and separated flow regions, and all simulations converge to the same level by $x/c \approx 1.5$.

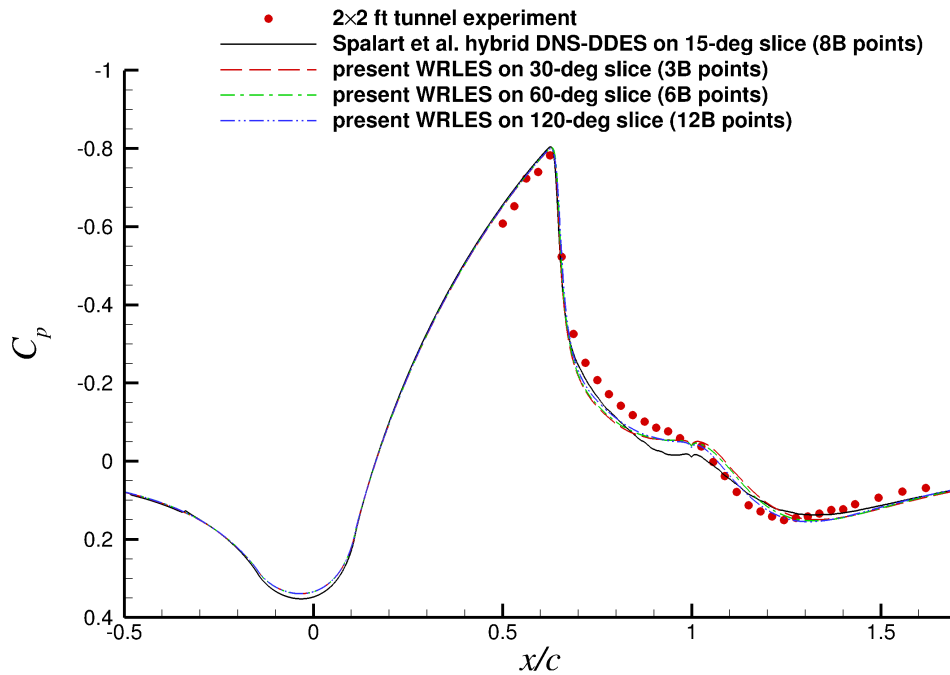
Figure 9(b) shows the C_f predictions of the three WRLES solutions and the comparison with the hybrid DNS-DDES data. The result from a RANS calculation with the SST-2003 model is also included. By extracting the streamwise locations at which C_f is zero, we can determine the separation and reattachment locations for each case. We see that all WRLES cases as well as the hybrid DNS-DDES of Spalart et al.^{8,9} predict the separation point at $x/c \approx 0.7$, which is the same as the separation point observed in the 2×2 ft tunnel experiment. RANS, on the other hand, is found to predict a somewhat earlier separation point at $x/c \approx 0.65$.

All cases except the RANS also capture a small spike in C_f at the trailing edge, which is caused by the sharp change in curvature at the junction of the bump and cylinder surface since no fillet was used at the trailing edge. We also observe in figure 9(b) that although the azimuthal span has a negligible effect on the C_f upstream of $x/c \approx 1$, its effect is more noticeable on the flow reattachment location and downstream region C_f . There is an upstream shift in the reattachment location as the azimuthal span is progressively increased from 30 to 60 to 120 degrees, with differences also observed in C_f levels downstream of the reattachment point. We see that the predicted reattachment point in the 120-degree WRLES (the most accurate value on the baseline grid) is at around $x/c \approx 1.16$, while the reattachment location in the 2×2 ft tunnel experiment was determined to be at around $x/c \approx 1.1$ from the surface oil flow measurement. Thus, the computed reattachment location is closer to the value of 1.17 observed in the 6×6 ft tunnel. This is understandable as the wind tunnel wall effects tend to diminish for the larger tunnel and our computation in free air becomes more relevant.

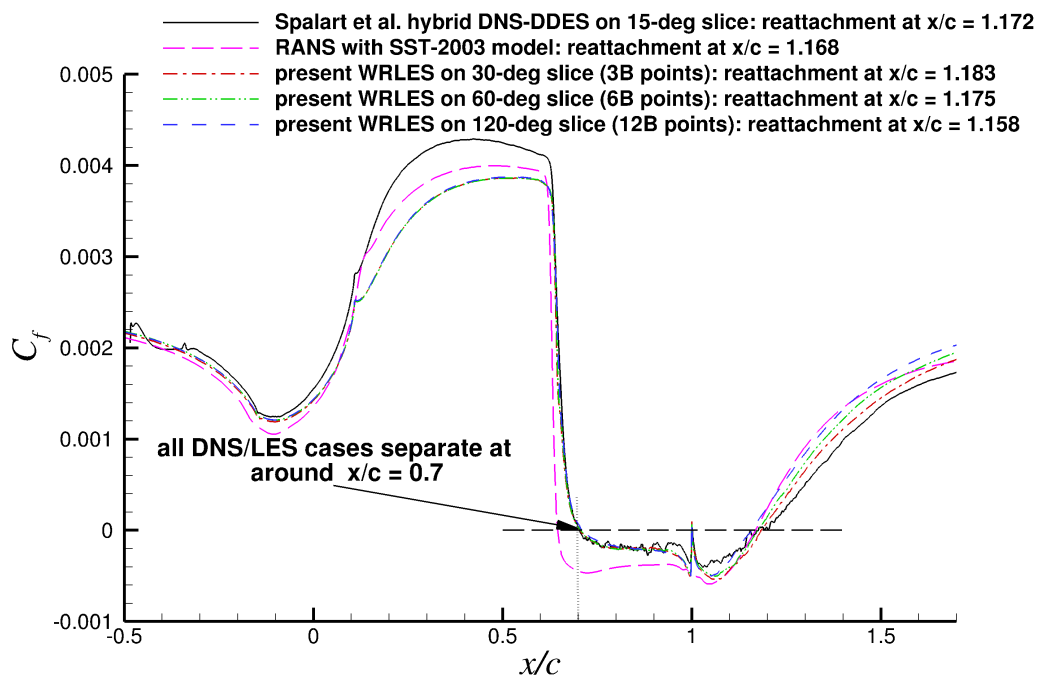
Another observation made from figure 9(b) is that the peak C_f levels observed prior to flow separation are significantly lower in the present WRLES than those in the hybrid DNS-DDES. The grid resolution in the attached region is clearly higher in the hybrid simulation since it employs DNS in that region. The DNS wall-normal grid spacing on the wall is about one half of that in the WRLES (note that the first grid off the wall in the WRLES still satisfies $r^+ < 1$), but the time step of the DNS is nearly thrice the value in the WRLES. Hence, the CFL number in the cells next to the wall in the DNS is about 6 times larger than that in the WRLES. Another difference between the WRLES and the DNS is the fact that the near-wall streamwise and spanwise grid resolutions in our baseline grid are coarsened by a factor of two in the outer boundary layer region using overset grids, as discussed earlier in section III.B. The effects of further grid refinement in the outer region and time step reduction are studied next.

3. Effect of Grid Resolution on C_p and C_f

The effect of grid resolution on the computed results is now examined. For this purpose, the 120-degree span case is repeated with the refined grid resolution, the details of which were provided in section III.B. This grid has 24 billion points total. The results of this case are compared with the results of the baseline grid 120-degree span case, which



(a) C_p distributions.



(b) C_f distributions.

Figure 9. Pressure coefficient (C_p) and skin-friction coefficient (C_f) comparisons.

contains 12 billion grid points total. The 24 billion point case and the 12 billion point case have been time-averaged over 7.5 and 10 chord flow times, respectively. Although the 24 billion point case was time-averaged over a shorter period than the 12 billion point case (due to the computational resource limitations), we do not expect the flow statistics to dramatically change if the time-averaging were to be increased from 7.5 to 10 chord flow times for the 24 billion point case. Figure 10(a) shows the C_p comparison between the two cases and includes the data from both tunnel tests. Two sets of large tunnel C_p data were extracted separately from the relevant figures given in Horstman and Johnson²⁸ and Johnson.³⁰ The extracted large tunnel datasets are somewhat different from one another and we do not know the reason for this. Part of the difference may likely be the error introduced by graphically extracting the data from the two figures. Figure 10(a) shows that there is a noticeable difference in the shock position between the two facilities and some scatter in the post-shock region C_p exists as well.

As seen here, grid refinement is found to shift the predicted shock location upstream and bring it closer to the location observed in the large facility. This is, as noted before, because our simulation used characteristic freestream boundary conditions at the outer boundary that are more likely to replicate the large tunnel results. We see that in the post-shock region, the C_p distribution from the refined grid calculation lies within the experimental scatter. This is perhaps the best agreement that can be expected given the difference between the simulation in free air and the wind tunnel tests and the fact that experimental uncertainties are not reported. Recall that we also do not know whether the simulated model has the correct leading-edge fillet radius as in the actual experimental model. As noted earlier, the leading-edge surface curvature determines how fast the flow accelerates over the front portion of the bump and therefore might affect the flow development further downstream.

Figure 10(b) shows the effect of grid resolution on the C_f distribution. In accordance with the upstream shift in the shock position on the refined grid, the separation point also shifts slightly upstream to $x/c \approx 0.69$. This is close to the separation point observed in the large tunnel. The reattachment point predicted on the refined grid remains nearly unchanged at $x/c \approx 1.16$, which is again close to the reattachment location observed in the large tunnel. We also observe a slight drop in the peak C_f level prior to separation.

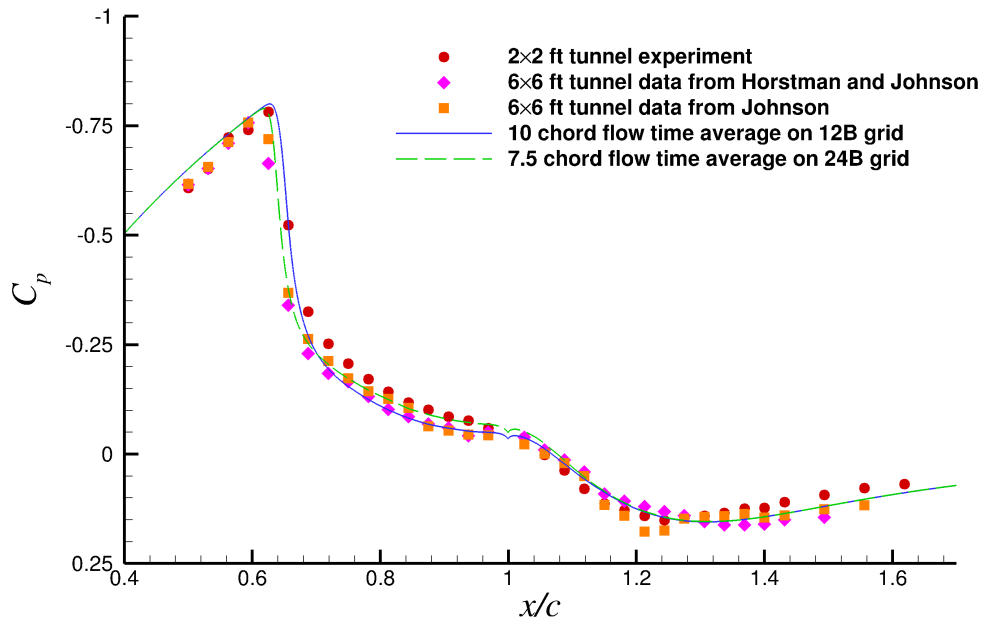
4. Effect of Time Step on C_p and C_f

We now investigate the effect of time step on the predictions. For this purpose, the 24 billion grid simulation is repeated at a time step of $\Delta t a_\infty/c = 2.5 \times 10^{-5}$, which is equal to one half of the original time step. The half time step case has been time averaged over 6.5 chord flow times while the original time step case has been averaged over 7.5 chord flow times. Figure 11 shows the time step effect on the C_p and C_f predictions. We see that the halved time step makes only a slight difference in the C_p prediction. A more significant impact is observed on the C_f prediction. At the half time step, the peak C_f level prior to flow separation drops by as much as 3.5% relative to the peak C_f value obtained at the original time step. Other than this difference, a very slight change in the separation point is observed and the reattachment point is nearly unchanged between the two cases.

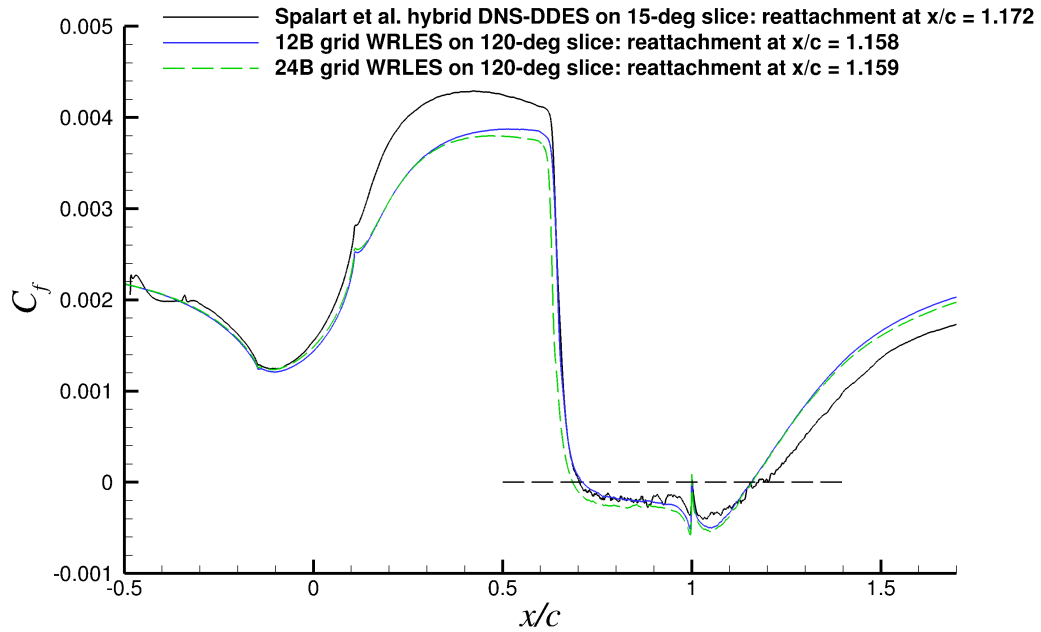
The best-resolved grid case (24 billion points on 120-degree span) at the half time step represents our most accurate result in this study as it is the result obtained with the highest resolution in space and time. The most accurate separation and reattachment points predicted in the present work are, respectively, $x/c \approx 0.69$ and 1.16. These predictions are in fair agreement with the corresponding values observed in the large tunnel experiment. Relative to the observation made in the large tunnel test, the error in the predicted separation-bubble length is on the order of 2-3%. We note that our time step of $\Delta t a_\infty/c = 2.5 \times 10^{-5}$ translates to a maximum value of $\Delta t^+ \approx 0.1$ in wall units. This value is observed in the peak C_f region prior to flow separation. The smallest time scale in the boundary layer is found in the viscous sublayer and is $\mathcal{O}(1)$ in wall units. The two time steps chosen in this study are therefore considerably smaller than the viscous time scale. To further investigate the C_f mismatch between the present result and that of Spalart et al.,^{8,9} we are currently studying the potential influence of the filter order of accuracy on the predictions. The findings from this ongoing study will be reported in the future.

5. Absence of Relaminarization in the Accelerating Flow Region

A strong favorable pressure gradient, commonly found over the leading edge of airfoils, can lead to the relaminarization of an incoming turbulent boundary layer if the flow acceleration caused by the favorable pressure gradient is sufficiently high. An interesting feature of the NASA wall-mounted hump flow studied previously^{10,11} is the flow acceleration over the front portion of the hump that is strong enough to exceed the relaminarization criterion of Narasimha and Sreenivasan³⁵ but only over a relatively short streamwise extent. It was previously observed¹¹ that while the flow did not relaminarize, the turbulent skin-friction variation exhibited a plateau, also observed in the experiment of Greenblatt et al.,³⁶ before it again began to rise.

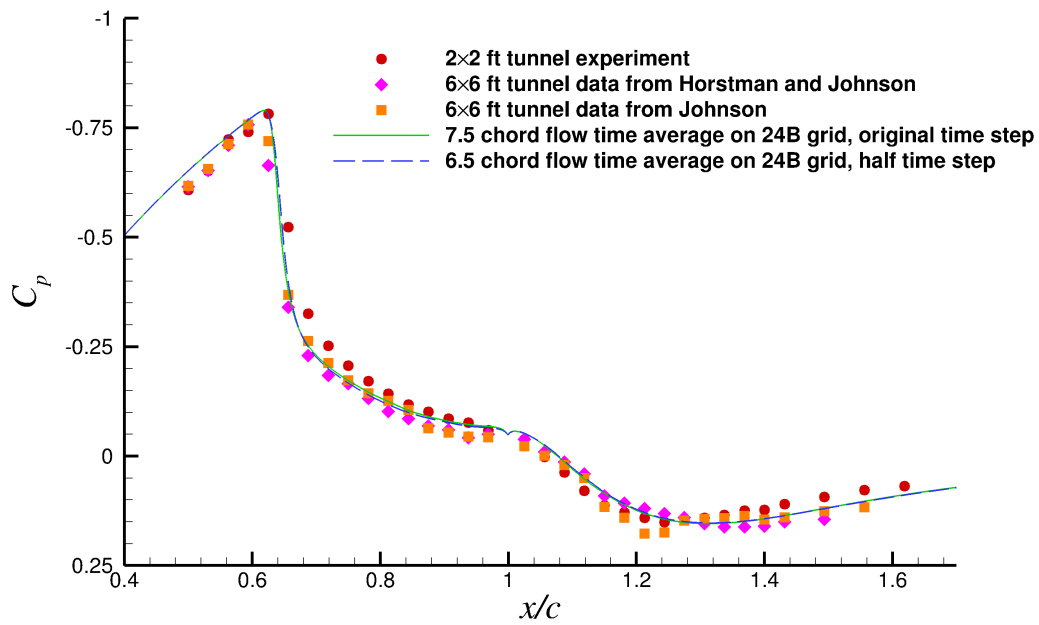


(a) C_p distributions.

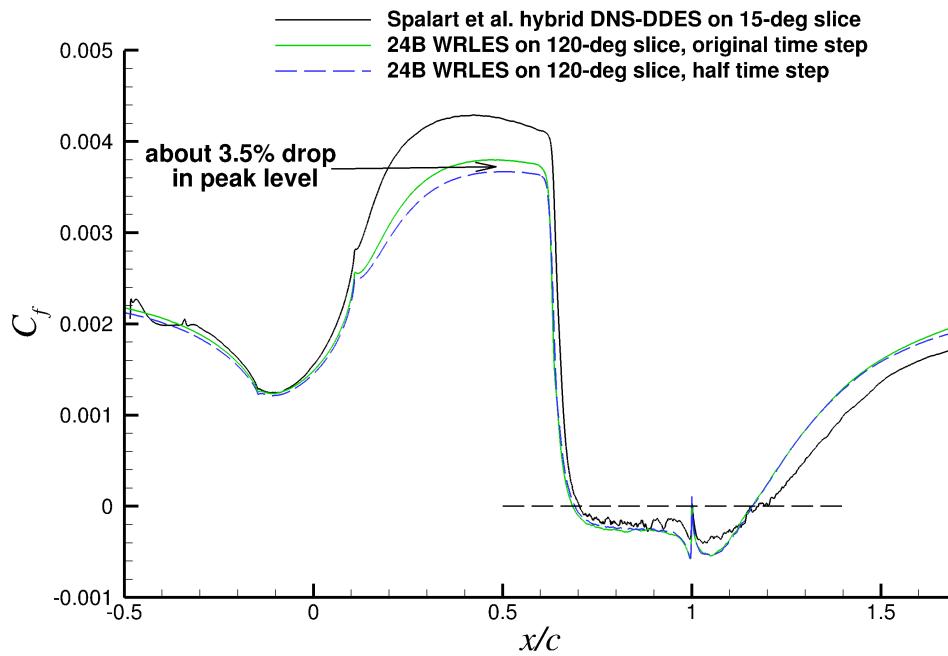


(b) C_f distributions.

Figure 10. Grid resolution effect on pressure coefficient (C_p) and skin-friction coefficient (C_f) distribution.



(a) C_p distributions.



(b) C_f distributions.

Figure 11. Time step effect on pressure coefficient (C_p) and skin-friction coefficient (C_f) distribution.

We observe no such plateau in the C_f distribution in the case of the transonic bump. To investigate the leading-edge region of the transonic bump in more detail, figure 12(a) plots the variation of the relaminarization parameter, K , for the transonic bump and compares it with the NASA wall hump. This figure reveals that the peak value in the present case is much lower than the relaminarization threshold, $K = 3 \times 10^{-6}$. To identify the reason for this, figure 12(b) shows the C_p comparison between the two cases. We see that the NASA wall hump clearly creates a stronger pressure gradient over the leading edge. At the same time, the chord-based Reynolds number is nearly 3 times higher for the transonic bump. The higher Reynolds number is obviously a deterrent against relaminarization. These main differences between the two cases therefore lead to a much lower peak K value in the case of the transonic bump.

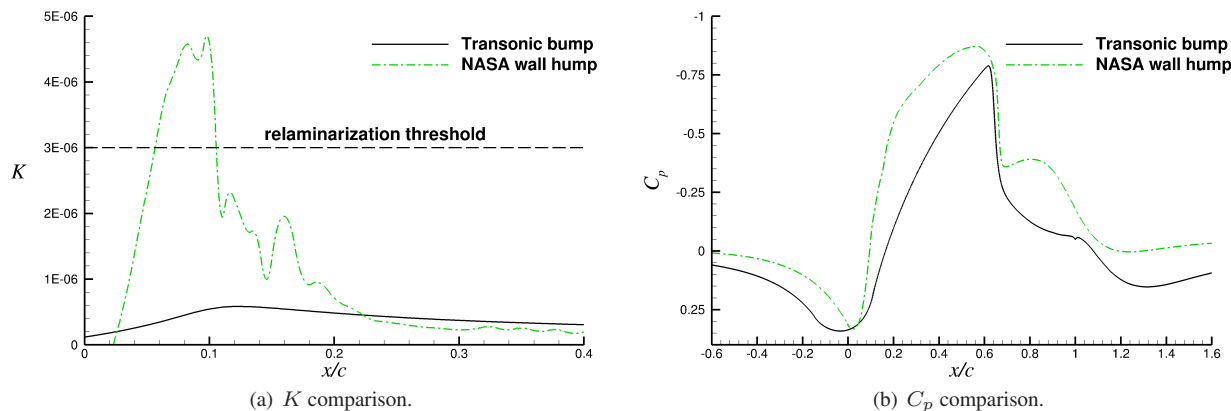


Figure 12. Relaminarization parameter, K , and C_p comparison between the transonic bump and the NASA wall hump.

6. Two-Point Correlations Along the Span

Next, we examine the two-point correlations along the span at two axial stations to investigate whether a sufficiently wide span has been used in the simulation. The normalized correlations based on the streamwise velocity fluctuations are computed using the following expression:

$$R_{u'u'}(x, r, \Delta\theta) = \frac{\langle u'(x, r, \theta) \cdot u'(x, r, \theta + \Delta\theta) \rangle}{\langle u'(x, r, \theta) \cdot u'(x, r, \theta) \rangle} \quad (2)$$

where u' denotes the streamwise velocity fluctuation, $\Delta\theta$ is the azimuthal separation between the two points and the $\langle \rangle$ operator denotes averaging in time. The correlations at a given (x, r) are first computed separately for each individual azimuthal point. Note that spanwise periodicity is assumed over 120 degrees of azimuth, thus the data is duplicated accordingly when $(\theta + \Delta\theta)$ in the above expression exceeds 120 degrees while θ is varied from 0 to 120 degrees. The maximum value of $\Delta\theta$ is half of the azimuth or 60 degrees. All of the individual correlations are then averaged to obtain a single correlation distribution.

The unsteady time history of the flowfield data gathered from our most accurate WRLES (24 billion point grid with 120-degree slice at the half time step case) is used in the calculation of the correlations shown here. Figure 13 shows the correlations in the attached region at $x/c = 0.5$ for various radial distances from the wall. As seen here, the correlations generally decay quickly. These correlations were calculated using the data gathered over about 4 chord flow times. A longer time average should flatten the oscillatory behavior observed around zero after the initial decay. The correlations approach zero by about $\Delta\theta \approx 10$ degrees, which implies that an azimuthal span of at least 20 degrees (i.e., twice the $\Delta\theta$) is needed in the attached region. We conclude from figure 13 that the chosen 120-degree azimuthal span is more than adequate in the attached region.

Figure 14 shows the correlations at $x/c = 1.2$, located slightly downstream of the reattachment point. The large structures generated in the separated shear layer region reattach without losing much of their coherence, thus this particular station represents a reasonable location to examine the longest-range azimuthal correlations. We plot the 2 and 4 chord flow time averages at this location for various radial distances from the wall. The difference observed between the two time averages suggests that a longer time average is needed for convergence. These correlations may

approach zero at midspan (60 degrees) with a longer time sample and this remains to be seen. The separated shear layer gives rise to the formation of large structures and hence the correlations in the separated/reattachment region decay over a larger azimuthal distance. These findings help explain why the reattachment point shifts upstream with the increased azimuthal span. The narrower azimuthal spans (30 and 60 degree slices) constrain the development of large structures in the separated region, and thus directly affect the growth rate of the separated shear layer and its reattachment location. The observations made from figure 14 suggest that the 120-degree azimuthal span might be just enough for the present problem.

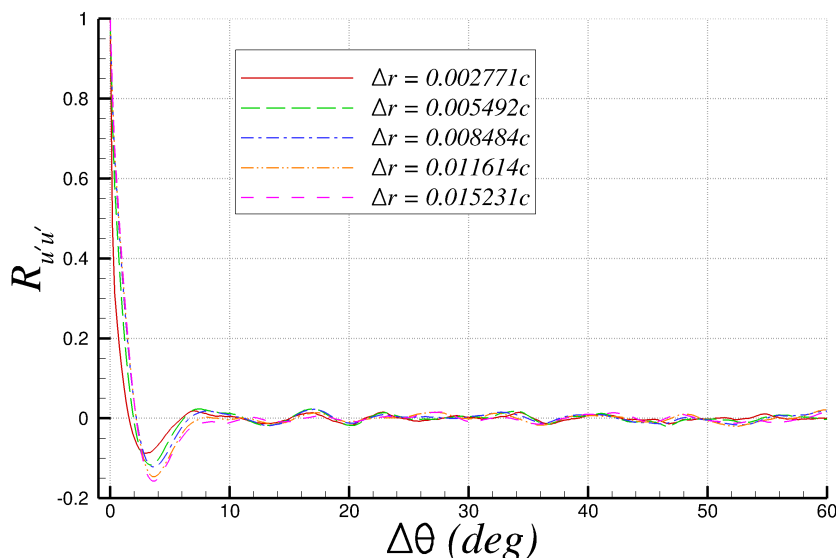
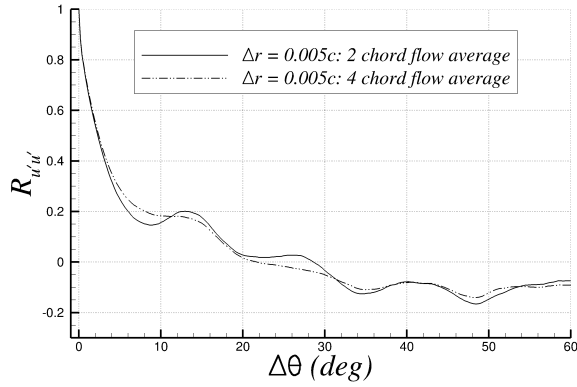


Figure 13. Two-point correlations of streamwise velocity fluctuations along the azimuthal span at $x/c = 0.5$.

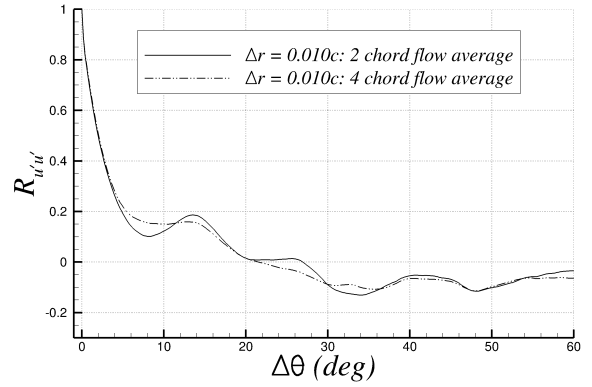
7. Further Comparisons with the Small Tunnel Data

We now examine the mean axial velocity profile and Reynolds shear stress profiles extracted at several axial stations from three 120-degree slice WRLES cases and the comparisons with the corresponding experimental measurements taken in the 2×2 ft tunnel. The computational results to be shown include the baseline grid (12 billion points) case at the original time step, and the refined grid (24 billion points) cases at the original and half time steps. As noted earlier, a comparison of the experimental measurements taken in the two facilities reveals that the separated flow reattaches sooner in the smaller tunnel. Because of the missing tunnel wall effects in the simulations, the comparisons to be made with the data taken in the small tunnel will only be qualitative in nature. These comparisons are shown in figures 15 and 16. In these figures, y' denotes the vertical distance measured from the wall, u and v are the axial and vertical velocity components, respectively, and the $\langle \rangle$ operator denotes averaging in time and along the azimuthal span. The superscript $'$ on u or v denotes the velocity fluctuation.

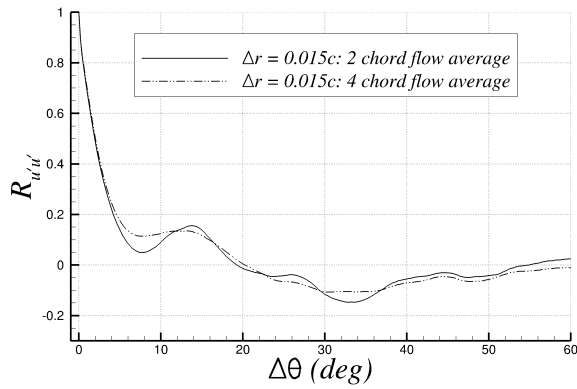
The first axial station is located upstream of the bump leading edge, at $x/c = -0.25$, while the remaining ones are located within the separation bubble and the reattachment region. The velocity profile comparison at $x/c = -0.25$ shows reasonable agreement with the experiment and provides confidence in the upstream conditions imposed in the simulation. We see that neither the increased grid resolution nor the halved time step has a significant effect on the mean velocity profile at this station. The velocity profile comparisons at the next three axial stations, which are located within the separation bubble until $x/c = 1$, display a greater impact of the increased grid resolution. Recall that the grid refinement causes an upstream shift in the shock position, which then leads to an earlier flow separation. The earlier flow separation on the refined grid is thus responsible for the differences seen in the reversed flow region within the separation bubble, particularly near the wall. Some effect of the increased grid resolution is also evident in the outer region. We also see that the halved time step effect on the velocity profiles at these three stations is rather minimal. These profiles generally display reasonable similarity to the experiment. Because of the delayed reattachment in all calculations relative to the small tunnel experiment, the comparisons in the vicinity of the experimental reattachment



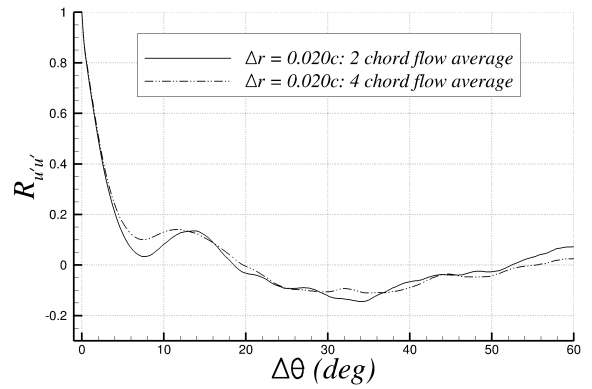
(a) $\Delta r = 0.005c$



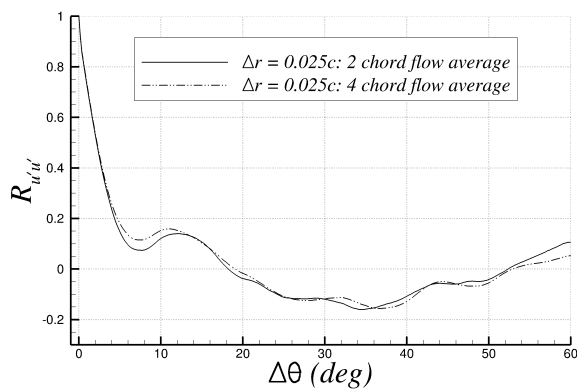
(b) $\Delta r = 0.010c$



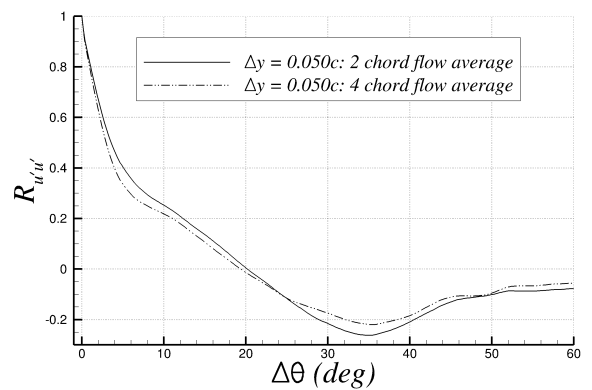
(c) $\Delta r = 0.015c$



(d) $\Delta r = 0.020c$



(e) $\Delta r = 0.025c$



(f) $\Delta r = 0.050c$

Figure 14. Two-point correlations of streamwise velocity fluctuations along the azimuthal span at $x/c = 1.2$.

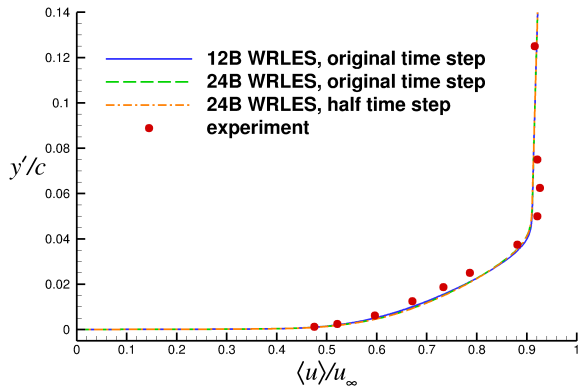
location and downstream show greater differences, as can be seen at $x/c = 1.125$ and 1.25 . We see that the grid refinement only has a modest effect at these two stations while the time step effect is again minimal.

Reynolds shear stress comparisons at the same axial stations depict generally similar qualitative behavior between the simulations and the experiment, but there are significant differences in the peak values at some stations. To our knowledge, there was no estimate provided for the uncertainty/error in the experimental dataset that was acquired nearly 4 decades ago. The comparison at the first station shows that the grid refinement slightly increases the peak Reynolds shear stress while the reduced time step slightly lowers it. The 24 billion grid case at the half time step represents our most accurate result. The peak Reynolds shear stress predicted in this calculation is about 26% lower than that in the experiment at this station. The comparisons at the other stations reveal a similar trend, in which the grid refinement generally tends to increase the peak shear stress level while the reduced time step tends to lower it, with the decrease being more prominent at some stations than at others. The agreement in the peak level between the simulation and the experiment is encouraging at $x/c = 0.813$. This station represents a relatively early stage in the evolution of the separated flow. As we traverse further downstream in the separated region, the difference in the peak shear stress levels between our most accurate result and the experiment becomes as much as 31%. The earlier flow reattachment in the small tunnel experiment suggests a faster growth of the separated shear layer relative to that in the simulation. The higher peak stress levels observed in the experiment would correlate well with the faster shear layer growth. Both the simulation and the experiment are in the reattached flow regime by $x/c = 1.25$, where we once again see a reasonable agreement between the computed and measured peak stress levels. However, this is likely fortuitous given the delayed reattachment point in the computation. The velocity profile comparison at the same station depicts a considerable difference between the two. Finally, we note that the hybrid DNS-DDES of Spalart et al.^{8,9} also showed a similar underprediction in the Reynolds shear stress comparisons, which were provided at $x/c = -0.25$ and 0.938 in their paper.

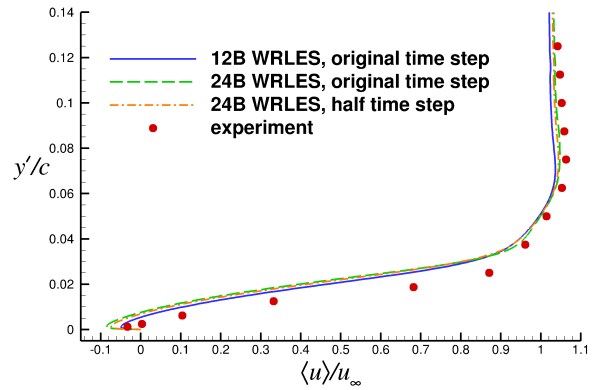
IV. Conclusions

A number of wall-resolved large eddy simulations have been performed for the Bachalo and Johnson flow experiment, which investigates the shock-induced boundary layer separation over an axisymmetric bump that is representative of the upper surface of a transonic airfoil. The high Reynolds number of the problem makes the wall-resolved simulations very challenging and requires billions of grid points. Simulations on grids containing as many as 24 billion points have been performed. The effects of domain span, grid resolution and time step on the simulation predictions have been examined. The predicted reattachment point of the separated flow is found to be sensitive to the azimuthal span chosen in the calculation. The predicted shock location in the aft region of the bump is found to shift upstream with further grid refinement in the vicinity of the shock. Halving the computational time step is found to decrease the peak skin-friction levels prior to flow separation and also lower the peak Reynolds stress levels observed in the separated region. A comparison of the experimental measurements taken in the two facilities revealed that the separated flow reattaches sooner in the smaller tunnel. This issue makes the direct comparisons with the 2×2 ft transonic tunnel measurements rather difficult as the present simulations do not model the tunnel wall effects. Nevertheless, the most accurately predicted separation and reattachment locations in the present study agree well with the limited measurements obtained separately in the 6×6 ft supersonic tunnel with solid walls. The most accurate surface pressure distribution obtained in this study lies within the experimental scatter of the measurements taken in the two facilities. The ILES results presented in this paper have been obtained using a sixth-order filter. Work is currently underway to evaluate the stability of higher-order filters on the present grids and determine the sensitivity of results to the filter order of accuracy. These findings will be reported in the future.

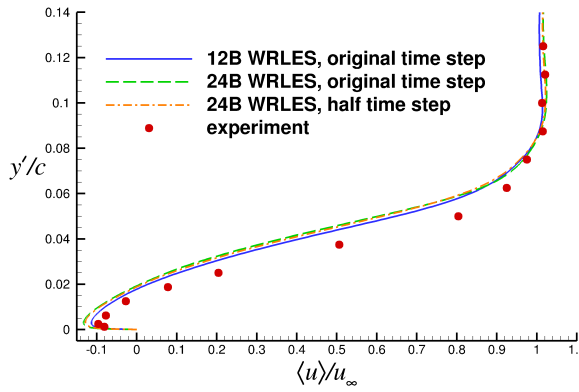
Because of the issues identified in the original experiment, we hope that this test case will be carefully repeated in a large facility in the near future and such a new test will provide additional detailed data for comparison with the computational predictions. As there is an uncertainty in the original geometry details, it is highly desirable that any new experimental investigation of this test case is based on the same geometry used in the present work so that meaningful comparisons between our computational study and the new experimental measurements can be made. The coordinates of the bump geometry used in this study are available to interested researchers.



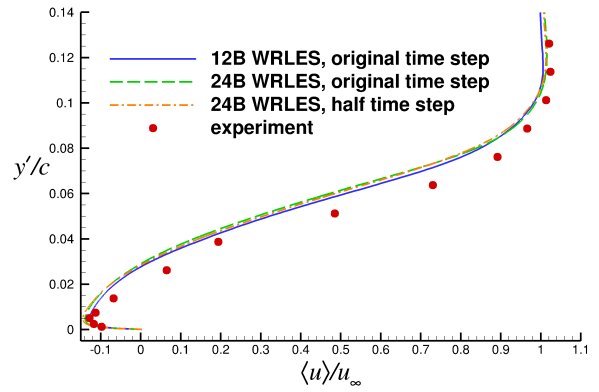
(a) $x/c = -0.25$



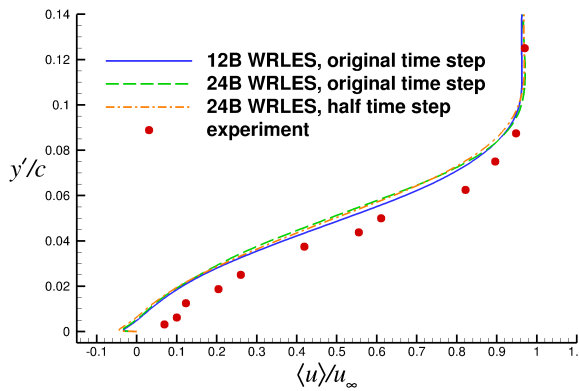
(b) $x/c = 0.813$



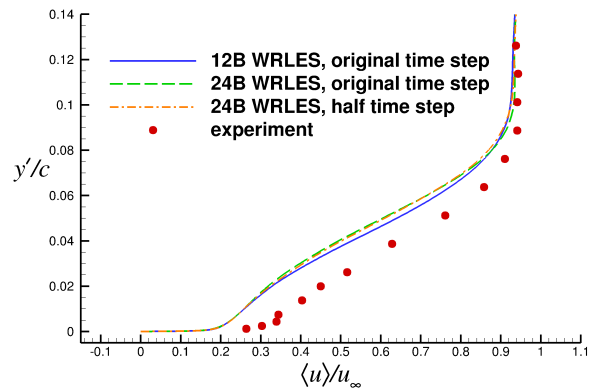
(c) $x/c = 0.938$



(d) $x/c = 1$

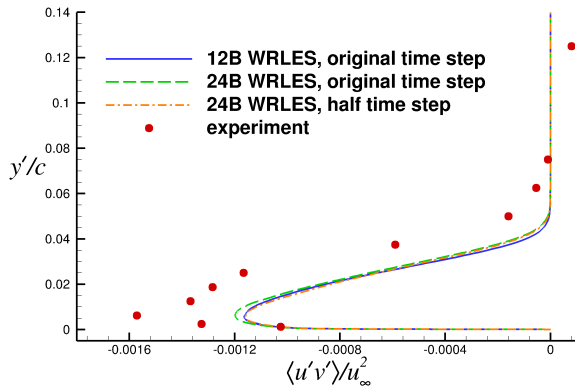


(e) $x/c = 1.125$

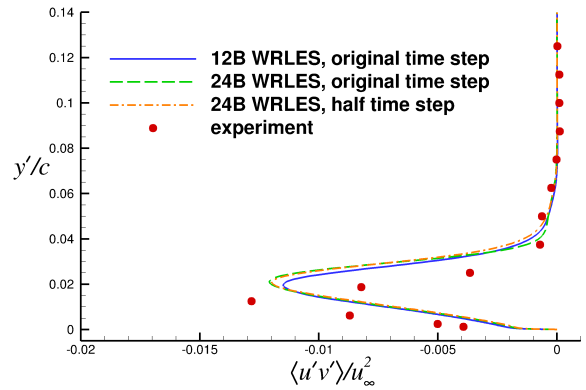


(f) $x/c = 1.25$

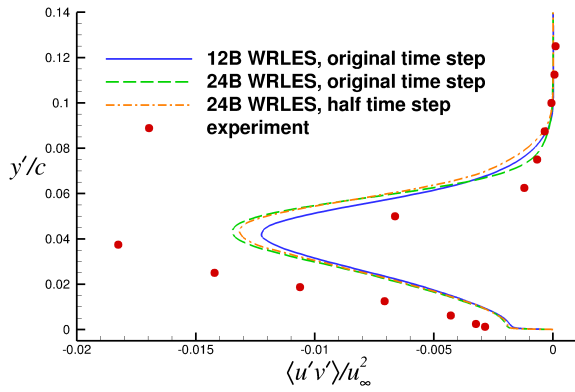
Figure 15. Mean axial velocity profile comparisons with the measurements taken in the 2×2 ft tunnel.



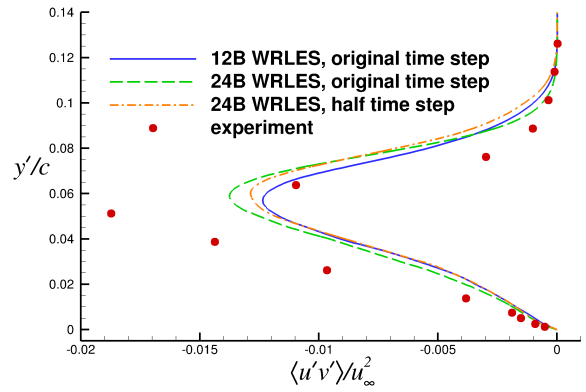
(a) $x/c = -0.25$



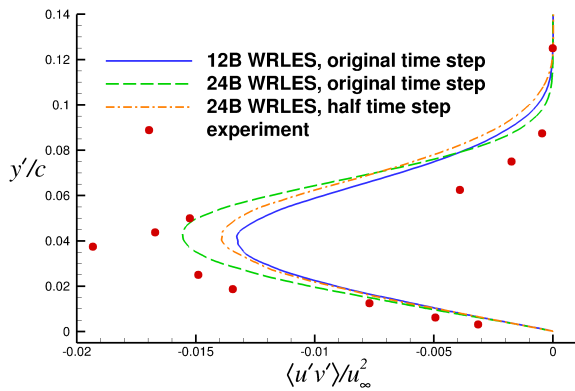
(b) $x/c = 0.813$



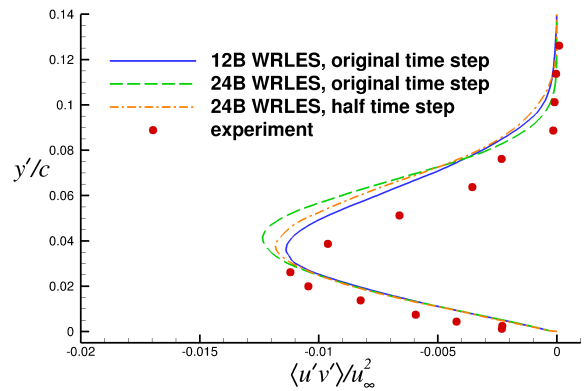
(c) $x/c = 0.938$



(d) $x/c = 1$



(e) $x/c = 1.125$



(f) $x/c = 1.25$

Figure 16. Reynolds shear stress profile comparisons with the measurements taken in the 2×2 ft tunnel.

Acknowledgments

This work was sponsored by the NASA Transformational Tools and Technologies Project of the Transformative Aeronautics Concepts Program under the Aeronautics Research Mission Directorate. This research used resources of the National Energy Research Scientific Computing Center, a DOE Office of Science User Facility supported by the Office of Science of the U.S. Department of Energy under Contract No. DE-AC02-05CH11231. The access to computational resources were provided under the 2016 and 2017 DOE ALCC programs. We acknowledge and very much appreciate useful discussions with Philippe Spalart, Michael Strelets and Dennis Johnson.

References

- ¹Rumsey, C. L., Gatski, T. B., Sellers III, W. L., Vasta, V. N., and Viken, S. A., "Summary of the 2004 Computational Fluid Dynamics Validation Workshop on Synthetic Jets," *AIAA Journal*, Vol. 44, No. 2, 2006, pp. 194–207.
- ²Avdis, A., Lardeau, S., and Leschziner, M., "Large Eddy Simulation of Separated Flow over a Two-Dimensional Hump with and without Control by Means of a Synthetic Slot-Jet," *Flow, Turbulence and Combustion*, Vol. 83, No. 3, 2009, pp. 343–370.
- ³Shur, M. L., Spalart, P. R., Strelets, M. K., and Travin, A. K., "Synthetic Turbulence Generators for RANS-LES Interfaces in Zonal Simulations of Aerodynamic and Aeroacoustic Problems," *Flow, Turbulence and Combustion*, Vol. 93, No. 1, 2014, pp. 63–92.
- ⁴Park, G. I., "Wall-Modeled Large-Eddy Simulation of a High Reynolds Number Separating and Reattaching Flow," Article in Advance, *AIAA Journal*, 2017.
- ⁵Duda, B. and Fares, E., "Application of a Lattice-Boltzmann Method to the Separated Flow Behind the NASA Hump," AIAA Paper 2016-1836, January 2016.
- ⁶Iyer, P. S. and Malik, M. R., "Wall-Modeled Large Eddy Simulation of Flow Over a Wall-Mounted Hump," AIAA Paper 2016-3186, June 2016.
- ⁷Bachalo, W. D. and Johnson, D. A., "Transonic, Turbulent Boundary-Layer Separation Generated on an Axisymmetric Flow Model," *AIAA Journal*, Vol. 24, No. 3, 1986, pp. 437–443.
- ⁸Spalart, P., Belyaev, K., Garbaruk, A., Shur, M., Strelets, M., and Travin, A., "Large-Eddy and Direct Numerical Simulations of the Bachalo-Johnson Flow with Shock-Induced Separation," 11th International ERCOFTAC Symposium on Engineering Turbulence Modelling and Measurements, Palermo, Italy, September 2016.
- ⁹Spalart, P. R., Belyaev, K. V., Garbaruk, A. V., Shur, M. L., Strelets, M. K., and Travin, A. K., "Large-Eddy and Direct Numerical Simulations of the Bachalo-Johnson Flow with Shock-Induced Separation," *Flow, Turbulence and Combustion*, Published online: 10 July 2017.
- ¹⁰Uzun, A. and Malik, M. R., "Wall-Resolved Large-Eddy Simulation of Flow Separation Over NASA Wall-Mounted Hump," AIAA Paper 2017-0538, January 2017.
- ¹¹Uzun, A. and Malik, M. R., "Large-Eddy Simulation of Flow over a Wall-Mounted Hump with Separation and Reattachment," *AIAA Journal*, (2017), accessed October 16, 2017. doi: <http://arc.aiaa.org/doi/10.2514/1.J056397>.
- ¹²Ashcroft, G. and Zhang, X., "Optimized Prefactored Compact Schemes," *Journal of Computational Physics*, Vol. 190, No. 2, 2003, pp. 459–477.
- ¹³Lele, S. K., "Compact Finite Difference Schemes with Spectral-like Resolution," *Journal of Computational Physics*, Vol. 103, No. 1, 1992, pp. 16–42.
- ¹⁴Gaitonde, D. V. and Visbal, M. R., "Padé-Type Higher-Order Boundary Filters for the Navier-Stokes Equations," *AIAA Journal*, Vol. 38, No. 11, 2000, pp. 2103–2112.
- ¹⁵Visbal, M. R. and Gaitonde, D. V., "Very High-Order Spatially Implicit Schemes for Computational Acoustics on Curvilinear Meshes," *Journal of Computational Acoustics*, Vol. 9, No. 4, 2001, pp. 1259–1286.
- ¹⁶Sherer, S. E. and Scott, J. N., "High-Order Compact Finite-Difference Methods on General Overset Grids," *Journal of Computational Physics*, Vol. 210, No. 2, 2005, pp. 459–496.
- ¹⁷Kim, J. W. and Lee, D. J., "Adaptive Nonlinear Artificial Dissipation Model for Computational Aeroacoustics," *AIAA Journal*, Vol. 39, No. 5, 2001, pp. 810–818.
- ¹⁸Ducros, F., Ferrand, V., Nicoud, F., Weber, C., Darracq, D., Gacherieu, C., and Poinso, T., "Large-Eddy Simulation of the Shock/Turbulence Interaction," *Journal of Computational Physics*, Vol. 152, No. 2, 1999, pp. 517–549.
- ¹⁹Ekaterinaris, J. A., "Implicit, High-Resolution, Compact Schemes for Gas Dynamics and Aeroacoustics," *Journal of Computational Physics*, Vol. 156, No. 2, 1999, pp. 272–299.
- ²⁰Uzun, A. and Hussaini, M. Y., "Investigation of High Frequency Noise Generation in the Near-Nozzle Region of a Jet Using Large Eddy Simulation," *Theoretical and Computational Fluid Dynamics*, Vol. 21, No. 4, 2007, pp. 291–321.
- ²¹Uzun, A. and Hussaini, M. Y., "Simulation of Noise Generation in Near-Nozzle Region of a Chevron Nozzle Jet," *AIAA Journal*, Vol. 47, No. 8, 2009, pp. 1793–1810.
- ²²Uzun, A., Bin, J., and Hussaini, M. Y., "High-Fidelity Numerical Simulation of a Chevron Nozzle Jet Flow," *International Journal of Aeroacoustics*, Vol. 10, No. 5&6, 2011, pp. 531–564.
- ²³Uzun, A. and Hussaini, M. Y., "Prediction of Noise Generated by a Round Nozzle Jet Flow Using Computational Aeroacoustics," *Journal of Computational Acoustics*, Vol. 19, No. 3, 2011, pp. 291–316.
- ²⁴Uzun, A., Hussaini, M. Y., and Streett, C. L., "Large-Eddy Simulation of a Wing Tip Vortex on Overset Grids," *AIAA Journal*, Vol. 44, No. 6, 2006, pp. 1229–1242.
- ²⁵Uzun, A., Kumar, R., Hussaini, M. Y., and Alvi, F. S., "Simulation of Tonal Noise Generation by Supersonic Impinging Jets," *AIAA Journal*, Vol. 51, No. 7, 2013, pp. 1593–1611.
- ²⁶Bachalo, W. D. and Johnson, D. A., "An Investigation of Transonic Turbulent Boundary Layer Separation Generated on an Axisymmetric Flow Model," AIAA Paper 79-1479, July 1979.

- ²⁷Johnson, D. A., Hortsman, C. C., and Bachalo, W. D., "Comparison Between Experiment and Prediction for a Transonic Turbulent Separated Flow," *AIAA Journal*, Vol. 20, No. 6, 1982, pp. 737–744.
- ²⁸Horstman, C. C. and Johnson, D. A., "Prediction of Transonic Separated Flows," *AIAA Journal*, Vol. 22, No. 7, 1984, pp. 1001–1003.
- ²⁹Johnson, D. A., "Predictions of Transonic Separated Flow with an Eddy-Viscosity/Reynolds-Shear-Stress Closure Model," AIAA Paper 85-1683, July 1985.
- ³⁰Johnson, D. A., "Transonic Separated Flow Predictions with an Eddy-Viscosity/Reynolds-Stress Closure Model," *AIAA Journal*, Vol. 25, No. 2, 1987, pp. 252–259.
- ³¹Morgan, B., Larsson, J., Kawai, S., and Lele, S. K., "Improving Low-Frequency Characteristics of Recycling/Rescaling Inflow Turbulence Generation," *AIAA Journal*, Vol. 49, No. 3, 2011, pp. 582–597.
- ³²Iyer, P. S., Private Communication, June 2017.
- ³³Schlichting, H., *Boundary-Layer Theory, Seventh Edition*, McGraw-Hill Book Company, 1979, pp. 569–570.
- ³⁴Klebanoff, P. S., "Characteristics of Turbulence in a Boundary Layer with Zero Pressure Gradient," NACA Report 1247, 1955.
- ³⁵Narasimha, R. and Sreenivasan, K. R., "Relaminarization in Highly Accelerated Turbulent Boundary Layers," *Journal of Fluid Mechanics*, Vol. 61, 1973, pp. 417–447.
- ³⁶Greenblatt, D., Paschal, K. B., Yao, C.-S., Harris, J., Schaeffler, N. W., and Washburn, A. E., "A Separation Control CFD Validation Test Case, Part 1: Baseline and Steady Suction," *AIAA Journal*, Vol. 44, No. 12, 2006, pp. 2820–2830.